Editorial

An update on liver chemical exchange saturation transfer imaging with a focus on clinical translation

Yì Xiáng J. Wáng[1]^, Weiqiang Dou[2], Zhiwei Shen[3], Yi Zhang[4]

[1]Department of Imaging and Interventional Radiology, Faculty of Medicine, The Chinese University of Hong Kong, Hong Kong SAR, China; [2]MR Research, GE Healthcare, Beijing, China; [3]Philips Healthcare, Beijing, China; [4]Key Laboratory for Biomedical Engineering of Ministry of Education, College of Biomedical Engineering & Instrument Science, Zhejiang University, Hangzhou, China

Correspondence to: Dr. Yi Xiang J. Wáng. Department of Imaging and Interventional Radiology, Faculty of Medicine, The Chinese University of Hong Kong, 30-32 Ngan Shing Street, Shatin, New Territories, Hong Kong SAR, China. Email: yixiang_wang@cuhk.edu.hk.

Submitted Mar 23, 2023. Accepted for publication May 15, 2023. Published online Jun 08, 2023.
doi: 10.21037/qims-23-379
View this article at: https://dx.doi.org/10.21037/qims-23-379

Introduction

Magnetization transfer (MT) imaging is a magnetic resonance imaging (MRI) technique that can be used to exploit the contrast between tissues where ^{1}H protons are present in three states: (I) bound to macromolecules, (II) in free water, (III) water in the hydration layer between the macromolecules and the free water (1). To assess MT, an off-resonance radiofrequency (RF) pulse is applied at a different frequency from the Larmor frequency of free-water protons. This pulse saturates protons bound to macromolecules but not those in free water. The saturated macromolecule-bound protons partially transfer their magnetization to protons in the hydration layer and free water. Some free water protons thus become saturated. When another excitation RF is applied, this time at the Larmor frequency of the free-water protons, the signal from the free water is reduced due to the pre-saturation of some free-water protons. The difference between the signals achieved with and without the off-resonance pulse can be compared and is referred to as the magnetization transfer ratio (MTR). In the early 1990s, Balaban and co-workers introduced chemical exchange saturation transfer (CEST) as a new type of contrast mechanism for MRI (2). In CEST imaging, the exchangeable protons in specific molecules are selectively saturated and, after transfer of this saturation by chemical exchange to water protons, detected indirectly through a signal change of bulk water (3-5).

Common species used for CEST imaging include exchangeable groups of -NH, -NH_2, and -OH, whose chemical shifts are ~3.5, ~1.8–3.0, and ~0.5–1.5 ppm from the water frequency, respectively. They are termed amide CEST, amine CEST, and hydroxyl CEST. Amide CEST is also popularly known as amide proton transfer (APT). The major known contributors to APT are the proteins and peptides of the tissue. In tumor regions, the concentration of proteins is elevated compared to surrounding tissues, and subsequently, the increased intracellular exchanges lead to an increased APT level. Zhou *et al.* (6) firstly investigated the feasibility of APT-weighted (APTw) imaging in the measurement of gliomas. The resultant APTw signal showed significantly higher value in the solid part than edematous or necrotic area in brain tumors. Moreover, low-grade brain tumors APTw imaging showed comparable effects with the surrounding tissues. Based on these findings in lesion assessment, APTw imaging has also been extensively applied to measure brain tumors with different grades, separate malignant tumors from other lesions such as edema, radiation necrosis, metastases, and monitor the tumor progression in malignant gliomas after clinical treatments (7-10). Glutamate (Glu) and creatine (Cr) are

^ ORCID: 0000-0001-5697-0717.

the two main metabolites with amine and guanidinium groups for CEST imaging, and thus are called GluCEST and CrCEST, respectively (11,12). Glu is a major excitatory neurotransmitter in the central nervous system. The concentration level of this metabolite is directly linked with multiple neurological and psychiatric diseases. The resultant GluCEST effect is generated and resides at about 3.0 ppm next to the water signal. The mobile protons in the hydroxyl group are also able to exchange with bulk water. Glycosaminoglycan (Gag) and glycogen are the two main metabolites with hydroxyl groups and have been investigated for CEST properties. Gag serves as a biomarker to evaluate the cartilage of knee or intervertebral discs. A low Gag concentration level is considered an indicator for early knee osteoarthritis and intervertebral disc degeneration (13,14). Glycogen, the major storage form of glucose in mammalian tissues, plays an essential role in systemic glucose homeostasis. Tumors often have an abnormally high reliance on the consumption of glucose, and glucoCEST is applied for imaging glucose. Due to the high abundance of glycogen in the liver, glycoCEST has been applied to monitor the glycogen in the liver. However, it should be noted that, although names like APT, glycoCEST, and gagCEST are being used, what this approach measures is often a 'weighted' CEST effect rather than a 'clean quantification'.

As CEST imaging is a much slower technique in data acquisition than other anatomical MRI techniques, it is firstly applied in brain lesions. Applying CEST to the liver is associated with many challenges, including, first of all, its acquisition is particularly susceptible to various physiological movements, mainly including respiratory motion and cardiac motion for the left liver. The liver is also more likely to be associated with susceptibility artifacts as it is close to the gas in the stomach and bilateral lungs. However, recent technological progress has allowed the successful implementation of CEST imaging in the liver, both for small animals in high-field magnets, as well as for human subjects in clinical scanners at 3.0 Tesla (T). GlycoCEST, APTw CEST, and tumor extracellular pH (pHe) measurement of the liver have been successfully reported. In tumor regions, the concentration of proteins is elevated compared to surrounding tissues, and subsequently, the increased intracellular exchanges lead to an increased APTw signal level. Compared with liver parenchyma, tumors with higher regeneration potential were noted to have higher APTw signal, and malignant liver tumors were shown to be acidic with lower pHe value. GlycoCEST measures liver glycogen level, with the liver at fasted status having a lower glycoCEST signal. Liver fibrosis leads to increased deposition of extracellular matrix proteins. Collagen, the major protein deposited in fibrosis, has a high content of amino acids, which forms amide bonds within the collagen structure. APTw CEST has been tested to assess liver fibrosis. This editorial summarises the reported applications of liver CEST imaging and discusses the technical innovations and challenges associated with liver CEST imaging.

Basic principle of CEST imaging

CEST allows the indirect measurement of low-concentration metabolites (μM to mM concentration range) by using exchangeable protons as the source for MRI contrast. For this transfer to take place, the chemical species in question must have in its structure a ^{1}H proton that is exchangeable with those of water. An RF pulse is applied at (one of) its resonant frequency(ies) to reach a saturation state. This magnetic saturation will spontaneously be transferred to water over time, via chemical exchange of the excited metabolite protons with non-excited water protons. The subsequent decrease in water signal, which can be detected by standard MRI sequences, provides an indirect measure for the concentration of the species of interest. Therefore, the core feature of CEST is the continuous transfer of saturated ^{1}H protons, leading to a build-up of saturation in water. When exchanging a saturated proton with water, that proton will be replaced with an unsaturated ^{1}H proton from water, which can in turn be saturated for another transfer. This exchange will take place at a rate that is affected by temperature and pH level and will continue until a steady state is reached (or until the end of the RF saturation).

The quantification of the CEST effect depends on measuring the water signal reduction caused by the saturation transfer, compared to the unsaturated image. For reliable CEST quantification, two competing effects, i.e., magnetization transfer contrast (MTC) and direct water saturation (DS), need to be eliminated. To achieve this, instead of comparing the signal reduction caused when saturating a specific spectral location (+τ ppm w.r.t. water) to that without saturation, the CEST effect is assessed by comparing with the water signal reduction when saturating the opposite spectral location (–τ ppm). This assumes that the MTC and DS effects are symmetrical regarding the water frequency (4):

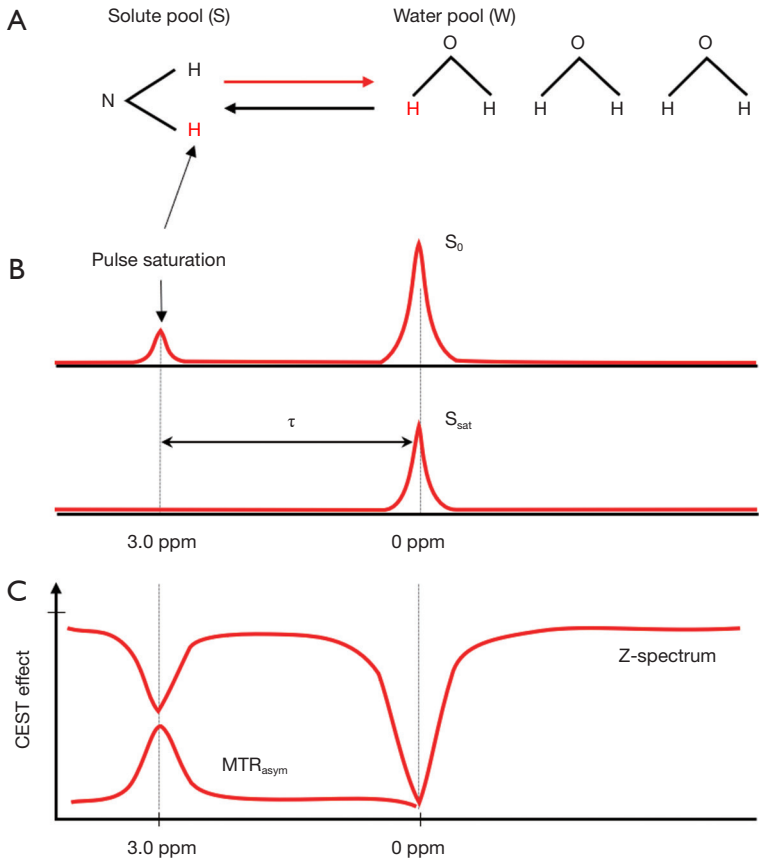

Figure 1 The schematic diagram of CEST. (A) The proton exchange between solute pool and water pool is shown. (B) After pulse saturation is applied at frequency of τ away from water peak, the water signal is decreased from S_0 to S_{sat} due to the proton exchange between solute and water pool. (C) A Z-spectrum is measured by normalizing water saturation (S_{sat}/S_0) over a series of saturation frequencies and the CEST effect was expressed quantitatively with MTR_{asym} which can be calculated by $S_{sat}(-\tau)/S_0 - S_{sat}(\tau)/S_0$ (C). CEST, chemical exchange saturation transfer; MTR_{asym}, asymmetrical magnetization transfer ratio.

$$MTR_{asym} = S(-\tau)/S_0 - S(\tau)/S_0 \quad [1]$$

where $S(\pm\tau)$ and S_0 denote the signal intensities obtained with the saturation RF pulse at the offset $\pm\tau$ and without the saturation pulse, respectively (*Figure 1*).

To derive the asymmetrical MTR parameter (MTR_{asym}) metric for an exchanging chemical compound at τ ppm, in theory, only CEST measurements at two opposite spectral locations plus a reference S_0 scan are needed. However, there is also an additional important confounding factor of magnetic field (B_0) inhomogeneity. The consequence of field inhomogeneity is a position-dependent shift of the entire spectrum, i.e., $S+\tau$ and $S-\tau$ are no longer at their assumed positions. To overcome this issue, knowledge of the frequency shift per voxel is needed so that all the measurements can be shifted back to their designated spectral positions. This can be achieved by densely sampling the spectral region around water (i.e., using RF saturation pulses at different frequency offsets around the expected frequency of water) and finding the minimal point after interpolation (i.e., where would be saturating the real frequency of water). In addition, regions around $+\tau$ and $-\tau$ also need to be densely sampled, so that the proper $S+\tau$ and $S-\tau$ may be recovered from the neighbouring points. With sparse sampling of the rest of the curve and proper interpolation, the so-called Z-spectrum is obtained. In practice, the saturation images at positive and negative offsets are acquired in an interleaved fashion.

APTw imaging is till now the most widely used type of CEST imaging based on the chemical exchange of amide (-NH) protons, and can reflect the concentration of endogenous mobile proteins or peptides, and pH

dependency. In APTw imaging, amide protons of peptides and proteins are selectively saturated using a specific RF pulse (3.5 ppm). Therefore, an asymmetric signal decrease of bulk water at an offset frequency of ±3.5 ppm can indirectly reflect the concentrations of endogenous mobile proteins and peptides.

The MTR_{asym} is the simplest to compute and the most widely used. However, the scale of the CEST effects generally encountered is small (<5% at 3.0 T), and the MTC effects for frequency ranges in close proximity to water (within 5 ppm) have been reported to be asymmetrical. The exact origin of this intrinsic asymmetry of MT is not completely clear. The nuclear Overhauser effect (NOE), the transfer of nuclear spin polarization from one nuclear spin population to another via cross-relaxation, and chemical exchange have been suggested as two important MTC pathways (15). This upfield NOE signal is a confounding factor for the quantification of downfield APT and other CEST effects. Thus, the MTR_{asym} image at 3.5 ppm is named APTw image rather than pure APT map, as this MTR_{asym} (3.5 ppm) includes certain other contributions. One possible method to mitigate the effects of asymmetric MTC is to compare the CEST effects between the target tissue and control tissue, as the asymmetric MTC effects may still be comparable. NOE effects can be lessened using higher RF amplitude (>2.0 μT) (16-18), and/or using models taking into account different exchange pathways.

Physiological factors, including tissue relaxation rates, pH value, and temperature, can also affect the CEST measurement. Another challenge for reproducible CEST measurements in practice is the completeness of the chemical exchange process. Ideally, measurement should be made after the two-way exchange process has reached a steady state. However, most *in vivo* CEST experiments have been made in the transient state, due to the impractically long RF saturation period needed to reach a steady state (>3 s at 3.0 T). Since the CEST effect depends on the RF saturation duration and relaxation delay which need to be long to reach its steady state, Sun (19) proposed the QUAsi-Steady State (QUASS) CEST method which allows shorter saturation and relaxation delay times. With this method, the evolution of the CEST signal is modelled as a function of the bulk water longitudinal relaxation rate during the relaxation delay and spin-lock relaxation rate during the RF saturation, from which the QUASS CEST effect is solved.

Furthermore, many instrumental and physiological factors influence the level of CEST effects. Localized high-order shimming is commonly performed for CEST imaging to reduce the static magnetic field inhomogeneity ΔB_0. MR pulse sequences for CEST imaging are composed of two parts: magnetization preparation and data acquisition. A large number of spectral offsets are required to adequately sample the Z-spectrum (>30 spectral points) and the long saturation time used (in the order of seconds) which lengthens the necessary repetition time (TR). For example, if a TR of 3 s is used and 40 spectral points are needed, the acquisition of a single slice will need at least 2 min (3*40), excluding calibration scans. Voxel-based quantification of CEST requires the alignment of all the images acquired at different spectral offsets, which limits CEST imaging of moving organs. Inhomogeneous B_0 field can cause the acquired Z-spectrum with chemical shift displacement, resulting in an erroneous assessment of the CEST effect, while imperfect B_1 power can lead to an insufficient saturation of the exchanging pool. To overcome these artefacts, several B_0 and B_1 correction methods have been proposed. One widely used B_0 correction method is to acquire an independent B_0 reference map in addition to the CEST measurement. The shifted Z-spectrum due to the imperfect B_0 field can thus be recovered accordingly. Water saturation shift reference (WASSR) is another B_0 correction method (20). With a weak and short B_1 power, a Z-spectrum dominated by direct saturation is generated and provides sub-Hertz accuracy for spectral frequency alignment. In addition, a combined B_1/B_0 correction method called water shift and B_1 (WASABI) had been proposed (21). Simultaneous B_0 and B_1 mapping can be acquired by using an off-resonant rectangular preparation pulse and applied for B_0 and B_1 correction in CEST imaging.

Chemical compounds with exchangeable protons can also be intravenously given to generate exogenous CEST effect. One typical example is glucose. A biodegradable CEST agent, D-glucose, has been administered into pathological lesions and measured dynamically with CEST imaging for exogenous contrast (22,23). In the meanwhile, chemical exchange-sensitive spin-lock (CESL) imaging (24), as a technique for T1rho weighted glucose enhanced imaging (glucoCESL), has also been applied to investigate the dynamic changes of injected D-glucose *in vivo* (25-27). In addition, some X-ray contrast agents such as iopamidol, iopromide, and Ioversol, are structured with amide exchangeable protons around the aromatic ring (also known as aryl amide), can generate CEST effects at unique frequencies (e.g., in the range of 4–6 ppm) which do not overlap with the frequencies of endogenous amide.

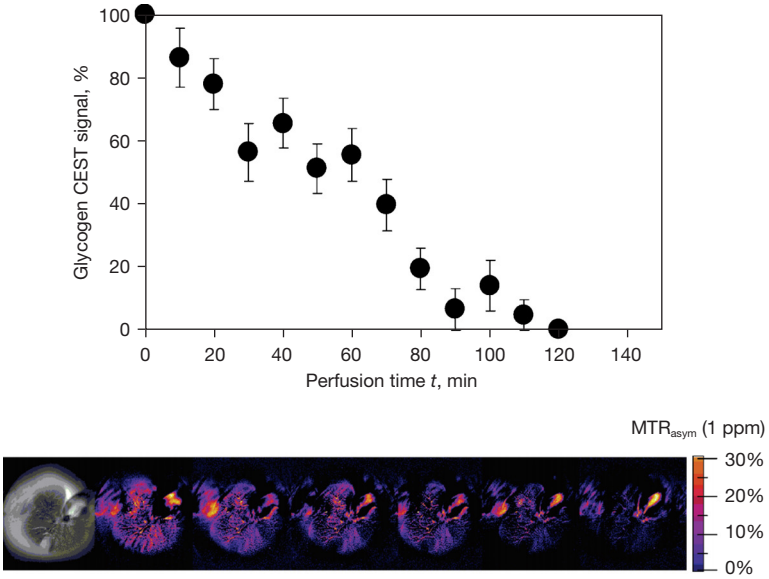

Figure 2 GlycoCEST imaging of a perfused fed-mouse liver at 4.7 T and 37 ℃ [modified with permission from van Zijl *et al.* (28)]. The first image (gray scale) marks the beginning of perfusion (t=0) with glucose-free media containing 500 pg/mL glucagon. The liver tissue is darkened because of the CEST effect from presaturation at 1.0 ppm for 1 s at 3.0 μT. The colorized glycoCEST images as a function of time during perfusion show the relative CEST intensity [MTR_{asym} (1 ppm)] of liver tissue as a function of perfusion time. The color scale shows that there are liver regions where the initial asymmetry difference between ±1.0 ppm is as high as 55% (orange pixels) and as low as 5% (blue pixels). With time, as glycogen disappears, the CEST images become more uniformly dark blue, corresponding to minimal glycogen. The corresponding glycogen depletion for a homogeneous region of interest is quantified in the top graph (n=4). CEST, chemical exchange saturation transfer; glycoCEST, glycogen CEST; MTR_{asym}, asymmetrical magnetization transfer ratio.

Due to the strong pH dependent CEST effect, these agents have been applied for tumor acidosis assessment and pH measurement in CEST imaging studies.

High-field preclinical study: liver glycoCEST

The earliest work of liver CEST imaging was reported by van Zijl *et al.* (28). In a seminal paper, van Zijl *et al.* showed that glycogen can be detected via CEST imaging of the hydroxyl protons in the 0.5- to 1.5-ppm frequency range downfield from water. Using a 4.7-T magnet, glycogen metabolism was followed in the isolated and perfused mouse livers before and after administration of glucagon. The imaging pulse sequence consisted of a Gaussian-shaped presaturation pulse followed by standard spin-echo imaging, with a series of spin-echo images collected from a single 3-mm slice of the liver after a 1 s presaturation pulse (B_1= 3 μT) applied at ±1 ppm. The intensity of the liver tissue was lower in images collected with a presaturation pulse turned on, compared with the image intensities in images without presaturation. When adding glucagon to the perfusate, the intensity of the saturated water signal at 1 ppm offset from water increased approximately 150% more during the 130-min perfusion period than the initial saturated water signal at 1 ppm. The difference in these intensities (MTR_{asym} at 1 ppm) decreased over a period of ≈120 min and remained constant thereafter. These final images represent the water intensity of a glycogen-depleted liver (*Figure 2*). Imaging the tissue distribution of glucose with spatial resolution has the potential to provide new insights regarding when and where glucose is produced, stored, transported, and used.

Sagiyama *et al.* (29) used glycoCEST imaging to detect liver glycogen in mice liver before and after fasting. For the phantom study, 100 mM glycogen in PBS and 100 and 200 mM of glycogen in 0.5% agarose were prepared at pH 7.4. MRI was conducted at 9.4 T. A train of Gaussian saturation pulses (B_1=9 μT, total 75 ms) were applied and followed by acquisition of a single line of k-space in linear ordering where the series of presaturation pulses result in maximal steady-state CEST at the center of the k-space for increased saturation efficiency. Images with the frequency

of the saturation pulse varied over 41 frequency offsets from 5 to −5 ppm with an interval of 0.25 ppm were collected. A reference image was obtained using a presaturation pulse set at 300 ppm. For the animal study, four mice were imaged before and after overnight fasting. After the second MRI scan, the animals were fed again for one day to recover, followed by a third MRI scan. Two phantoms with 100 mM glycogen in phosphate-buffered saline and 200 mM glycogen in 0.5% agarose were also placed beside the animals. The same CEST imaging sequence used in the phantom study was applied on a single 2 mm slice of the liver. Another set of CEST images in the same geometry were also obtained for WASSR B_0 correction. The MTR_{asym} map was generated at every 0.25 ppm for each animal. MTR_{asym} was also measured in the back muscles and the reference phantoms. Liver *in vivo* MTR_{asym} maps at 1.25 ppm showed a signal decrease after fasting and recovered after re-feeding. The mean MTR_{asym} at 1.25 ppm after fasting (1.66%±0.31%) became significantly lower compared to that before fasting (2.36%±0.16%), and it returned to the original level after re-feeding (2.37%±0.26%); while the signal of the back muscle remained low and constant. This study also showed that the detection of glycogen signal by glycoCEST is sensitive to temperature.

Using an 11.7-T magnet, Miller *et al.* (30) performed liver glycogen measurements with CEST imaging and then compared CEST results with measurements from interleaved ^{13}C nuclear magnetic resonance (NMR) spectra. CEST acquisitions were performed using 32 nonuniformly spaced frequency offsets: ±9, ±8.5, ±8, ±6, ±4, ±2.5, ±2, ±1.75, ±1.5, ±1.25, ±1, ±0.75, ±0.5, ±0.25, ±0.1, 0, and 40 ppm from water. Saturation pulse power and time for perfused liver studies were 4 μT and 0.5 s. It was noted that CEST-based glycogen measurements were highly correlated with ^{13}C NMR glycogen spectra. They found that the CEST signal from glycogen in the liver was significantly less than that observed from identical amounts in solution. Thus, they suggested that: (I) phantom solutions cannot be used to calibrate *in vivo* or whole tissue glycogen measurements, and (II) free glucose, despite its lower physiological concentration, could still significantly interfere with glycogen CEST measurement.

Ren *et al.* (31) reported a study with mouse livers perfused with a Eu^{3+}-based glucose sensor [EuDOTAM-bis(methyl)-bis(phenylboronate) (EuDOTAM-2M-2PB)] containing two phenylboronate moieties as the recognition site. This sensor contains the paramagnetic lanthanide ion, Eu^{3+}, chelated by a macrocyclic ligand containing a glucose recognition site, and has high binding affinity and selectivity toward glucose. For *in vivo* study, a liver was isolated from a fed mouse and perfused with buffer containing 10 mM EuDOTAM-2M-2PB and 10 mM glucose to mimic hyperglycemia. A second liver (to serve as a control) was removed from a 24-hour fasted mouse and perfused an equivalent amount of sensor but no glucose. Liver images were collected using a 4.7-T magnet. A Gaussian-shaped presaturation pulse was used with a duration of 2 s and the power level (B_1) of 1 kHz (23.5 μT). The saturation frequency was at the Eu^{3+}-bound water resonance frequency (42 ppm at 37 ℃, "on-resonance") and at 120 ppm ("off-resonance"). The CEST spectrum of the perfusate lacking glucose showed no clear exchange peak while the spectrum of the perfusate containing both glucose and agent showed a distinct CEST peak at the known Eu^{3+}-bound water position. Activation of the sensor by applying a frequency-selective presaturation pulse at 42 ppm resulted in a 17% decrease in water signal in livers perfused with 10 mM sensor and 10 mM glucose compared with livers with the same amount of sensor but without glucose. Livers perfused with 5 mM sensor but no glucose can detect glucose exported from hepatocytes after hormonal stimulation of glycogenolysis.

High-field preclinical study: assessing liver fibrosis with APTw CEST

Liver fibrosis results from the continuous presence of a harmful stimulant, which causes persistent hepatocyte injury that leads to chronic inflammation, hepatocyte death and regeneration, varying levels of fat deposition, and increased deposition of extracellular matrix proteins. Collagen, the major protein deposited in fibrosis, has a high content of amino acids, which form amide bonds within the collagen structure (32). Liver fibrosis changes the composition of the hepatic extracellular matrix, which includes increases in proteoglycans (33). As collagen levels increase, a commensurate increase in the number of amide protons in the tissue occurs. APTw imaging can detect amide protons and, therefore, may reflect the quantity of collagen present.

In a phantom study, Lindquist *et al.* (34) studied syringes filled with aqueous phantoms containing 0%, 2%, 5%, 10%, and 20% collagen at 7.0 T. Z-spectrum data were acquired using a gradient recalled echo (GRE) sequence, and a 15.6 μT/15 ms Gaussian saturation pulse with frequency offsets of 20, 10, 8, 6, 5, 4.5, 4, 3.8, 3.7, 3.6, 3.5, 3.4, 3.3, 3.2, 3.1, 3, 2.75, 2.5, 2.25, 2, 1.8, 1.6, 1.4, 1.2, 1, 0.5, and 0 ppm

from water. For *in vivo* study, male C57Bl/6 mice were used (n=8 for control and n=8 for CCl_4 insult), and liver fibrosis was induced with twice weekly intraperitoneal injections of CCl_4. MRI data were acquired at two time points, at 12 and at 16 weeks. Z-spectrum data were acquired using a single slice, a 15.6 μT/15 ms Gaussian saturation pulse with the same frequency offsets as used in the phantom study. For the raw Z-spectrum, 5-pool Lorentzian fits were calculated pixelwise for each of the components (amide, amine, MT, water, and nuclear Overhauser enhancement) of the Z-spectrum using a multi-Lorentzian function and the Levenberg-Marquardt algorithm.

Phantom showed increased APTs signal with increasing collagen concentration (R=0.97). APT in the left liver lobe was significantly greater for the CCl_4 treated animals than the controls at 16 weeks (8.0%±1.2% *vs.* 6.2%±1.0%; P=0.0058). The liver left lobe APTw signal at 16 weeks positively correlated with percent Sirius Red staining (% area, R=0.58, P=0.019) and also correlated with the hydroxyproline assay (μg/g, R=0.50, P=0.046).

High-field preclinical study: tumor pHe measurement

The pHe of the tumor microenvironment is typically acidic, in the range of 6.5 to 6.9, whereas the pHe of normal tissue is approximately 7.2 to 7.5 (35,36). Extracellular tumor acidosis is the result of increased lactic acid production by high aerobic glycolysis and poor perfusion of tumor cells. This resultant acidity can enhance tumor aggressiveness, metastasis, chromosomal rearrangements, and angiogenesis. Low pHe also leads to resistance to radiation treatment and specific chemotherapeutics (37). Given the association of acidity with tumor malignancy, accurate measurement of tumor pHe may aid in the identification of malignancy and tumor invasion, as well as in predicting therapeutic efficacy.

The CEST effects are modulated by several factors including pH, temperature, and contrast agent concentration (if administered). CEST contrast agents can map the pHe in the microenvironment in which they distribute (38). So-called 'ratiometric method' has been described for contrast agent enhanced CEST imaging to minimize the effect of contrast agent concentration (39). It has been noted that there is a higher CEST effect of ioversol due to its faster chemical exchange rate and higher accumulation than other iodinated contrast agents (40). Ioversol has two amide groups detected 4.3 ppm downfield from water and has different CEST effects at different RF power levels, allowing an RF power-based ratiometric method to rule out concentration effects.

In a rat study, Chen *et al.* (41) demonstrated that ioversol CEST MRI can be exploited to achieve pHe mapping of liver cancer. Firstly, with *in vitro* studies, Chen *et al.* prepared phantoms containing seven micro-centrifuge tubes with 30 mM ioversol in phosphate-buffered solution, titrated using HCl or NaOH, to various pH values ranging from 6.0 to 7.8. The other phantom contained six micro-centrifuge tubes of pH 7.2 ioversol, at concentrations from 10 to 60 mM, in phosphate-buffered solution. The phantoms were filled with agarose solution and solidified at 37 ℃. Experiments were performed on a 7.0-T scanner with images acquired using an echo-planar imaging (EPI) sequence. Continuous wave RF saturation was applied for 5 s, with RF irradiation powers of 1.5, 3, 6, and 9 μT for testing the CEST Z-spectra of phantoms. Z-spectra were obtained ranging from −8 to 8 ppm, at intervals of 0.31 ppm. CEST Z-spectra showed Ioversol exhibits a strong CEST signal with a peak at 4.3 ppm corresponding to the two exchangeable amide groups. With increasing pH, the signals increased due to the higher exchange rate. To quantify the CEST effects, the saturation transfer effect (ST%) was measured within a pH range of 6.0 to 7.8, using two saturation pulse powers (1.5 and 6 μT). The ratiometric value [RF power mismatch (RPM)] was calculated according to the following equation:

$$\mathrm{RPM} = \left[\left(1-\mathrm{ST}\right)/\mathrm{ST}_{\mathrm{RF1}}\right]/\left[\left(1-\mathrm{ST}\right)/\mathrm{ST}_{\mathrm{RF2}}\right] \quad [2]$$

where $ST_{RF1,2}$ are the saturation transfers obtained at two different powers (two different flip angles). The CEST effects with irradiation power of 6 and 1.5 μT both had the lowest value at pH 6.0. The CEST effects gradually increased with increasing pH, and reached the highest value at pH 7.5 at irradiation power of 6 μT and the highest value at pH 7.2 at irradiation power of 1.5 μT, and then began to decrease (*Figure 3*). This observation was similar to the report described by Longo *et al.* (42). Moreover, the pH map revealed no significant difference between various ioversol solutions. The RPM curve demonstrated that, in the pH range of 6.0 to 7.8, the $\log_{10}$ ratio of CEST effect and pH exhibited an excellent correlation (R^2=0.98) (*Figure 3*).

For *in vivo* imaging, McA-RH7777 rat hepatoma cell line was planted in the livers of 10 female SD rats. CEST images were acquired using an EPI sequence. Continuous

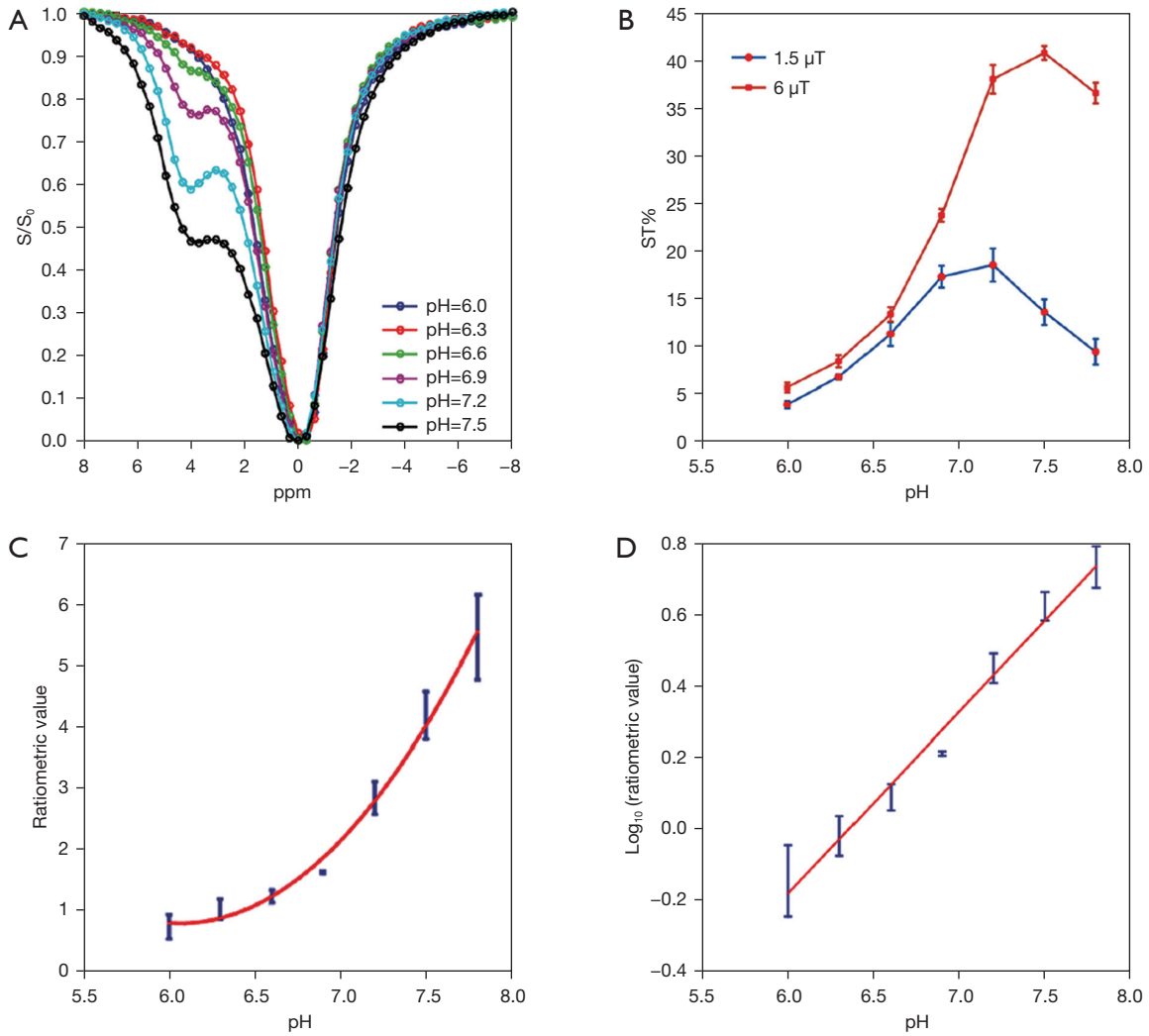

Figure 3 Ioversol exhibits a strong CEST signal [modified with permission from Chen *et al.* (41)]. (A) Z-spectra of 30 mM ioversol at different pH values at 6 μT. (B) Ioversol ST% depends on pH at RF saturation powers of 1.5 and 6 μT. (C) The CEST ratio was exponentially correlated with pH. (D) The $\log_{10}$ ratio of the CEST effect linearly correlated with pH. CEST, chemical exchange saturation transfer; RF, radiofrequency; ST, saturation transfer.

wave RF saturation was applied for 5 s, with RF irradiation powers of 1.5 and 6 μT for CEST imaging. Ioversol (4 g iodine/kg body weight) solution was injected via the tail vein, and CEST images were acquired at two RF power 1.5 and 6.0 μT, 15 min after ioversol injection. After ioversol administration, the liver tumor exhibited a lower CEST signal compared with the normal liver tissue, at both 1.5 and 6 μT irradiation. The pHe map distinguished tumor from normal tissue, and the pHe of the tumor was lower than that of normal liver tissue in all 10 rats (41).

Clinical 3.0-T scanner: rat liver APTw CEST and glycoCEST study

In 2016, Chen *et al.* (43) reported rat liver APTw CEST and glycoCEST studies using a 3.0-T Philips clinical scanner. CEST image acquisition was performed using a single-slice turbo spin-echo sequence with chemical shift-selective fat suppression. A continuous rectangular RF pulse was performed for saturation, with a B_1 field strength of 3 μT and a fixed duration of 300 ms. Baseline image was obtained first without using saturation pulse, and then the saturated

images were acquired at the offsets of 0, ±0.25, ±0.5, ±0.75, ±1, ±1.25, ±1.5, ±1.75, ±2, ±2.25, ±2.5, ±2.75, ±3, ±3.25, ±3.5, ±3.75, ±4, ±4.25, ±4.5, ±4.75, ±5 ppm. The total data acquisition time was 16 min and 31 s. The glycogen proton exchange rate is estimated to be faster than the amide proton exchange rate, so a slightly higher saturation strength of 3 μT was used in this study. Meanwhile, the longest saturation duration of 300 ms that was achievable on the used MRI scanner was applied to approach complete direct saturation. For Z-spectrum analysis, regions of interest (ROIs) were first manually placed on the liver parenchyma region to avoid artefacts and vessels. For each voxel, the Z spectrum was first least-square fitted by a 12th-order polynomial model and interpolated to a finer resolution of 0.001 ppm. The MTR_{asym} at 3.5 ppm was quantified as APTw value and the mean MTR_{asym} in the frequency range $\Delta\Omega$ =0.5 to 1.5 ppm was quantified as glycoCEST value.

For the fasting status study, eight rats were not fed rat chow for 24 hours. These rats were scanned twice before fasting and after fasting. Eleven rats underwent liver CCl_4 intoxication study (intraperitoneal injection of 1 mL/kg body weight). These rats were scanned before and 48 hours after CCl_4 administration. The post-fasting APTw value decreased from 2.38%±0.86% to 0.67%±1.12% (P=0.012). The mean glycoCEST measurement also decreased after fasting (0.34%±0.26% to −0.18%±0.37%, P=0.012). For the CCl_4 insult study, the baseline APTw value was 2.46%±0.48% and the glycoCEST value was 0.34%±0.23%, while 48-hour after CCl_4 injection, the liver APTw value reduced to 1.10%±0.77% (P=0.004), and the glycoCEST value reduced to −0.16%±0.51% (P=0.02) (*Figure 4*). This reduction of glycoCEST MTR_{asym} after fasting is believed to reflect the reduction of hepatic glycogen levels. In addition, there was a significant drop in glycoCEST MTR_{asym} in the CCl_4 intoxicated rat livers. According to Muriel (44) in the CCl_4 intoxicated rat liver, glycogen content decreased significantly compared to the normal liver. Forty-eight hours after CCl_4 intoxication, the liver is expected to be associated with a great extent of inflammation, oedema and tissue necrosis, and involves metabolic activation, reactive free radical metabolites, lipid peroxidation, covalent binding and disturbance of calcium homeostasis.

Clinical 3.0-T scanner: human liver APTw CEST and glycoCEST study on reproducibility and fasting effect

In 2016, Chen *et al.* (43) and Deng *et al.* (45) demonstrated the feasibility of liver CEST imaging using a 3.0-T Philips clinical MRI scanner. Deng *et al.* reported glycoCEST imaging for *in-vivo* human liver, where the glycoCEST signal would be much lower than that at the dedicated high-field MRI scanners for research. There were in total 15 healthy volunteers. Each volunteer underwent scans at two time points: 1.5–2 hours post-dinner and overnight (12-hour) fasting. In order to test the scan-rescan reproducibility of glycoCEST and APTw MRI, 7 out of 15 volunteers underwent scans twice additionally in the morning after light breakfast with a time interval of 7 days.

CEST images were acquired using a single-slice turbo spine echo sequence with chemical shift-selective fat suppression. A continuous-wave rectangular RF pulse was performed for saturation, with a B_1 field strength of 3 μT and a fixed duration of 300 ms. Baseline image was obtained first without using saturation pulse, and the saturated images were then acquired at the 41 offsets of 0, ±0.25, ±0.5, ±0.75, ±1, ±1.25, ±1.5, ±1.75, ±2, ±2.25, ±2.5, ±2.75, ±3, ±3.25, ±3.5, ±3.75, ±4, ±4.25, ±4.5, ±4.75, ±5 ppm. The images were acquired with a breath-hold technique. The total data acquisition time was 4 min and 58 s. For Z-spectrum analysis, the Z-spectrum was first least-square fitted by a 12th-order polynomial model and interpolated to a finer resolution of 0.001 ppm in each voxel. The MTR_{asym} at 3.5 ppm was quantified as APTw value and the mean MTR_{asym} in the frequency range $\Delta\Omega$ =0.5 to 1.5 ppm was quantified as glycoCEST value. ROI based measurements were manually conducted on liver parenchyma region excluding artifacts and blood vessels.

For glycoCEST, the intraclass correlation coefficient (ICC) value for scan-rescan reproducibility was 0.758, while for APTw the ICC value was 0.835. The results of post-meal and post-fasting glycoCEST and APTw measurements in 15 subjects are given in *Figure 5*. Compared with post-meal, both glycoCEST measurement and APTw measurement decreased post 12-hour fasting. Since the fat suppression was applied prior to the acquisition, this MTR_{asym} may not be dominated by the contamination of lipid at −3.5 ppm relative to water resonance (46). However, the glycoCEST signal at clinical field strength is more likely contaminated by direct saturation of water and other CEST pools resonating at proximate frequencies due to the smaller absolute chemical shift.

Clinical 3.0-T scanner: APTw CEST for liver tumors in human patients

Tumors generally show higher APT signals than normal

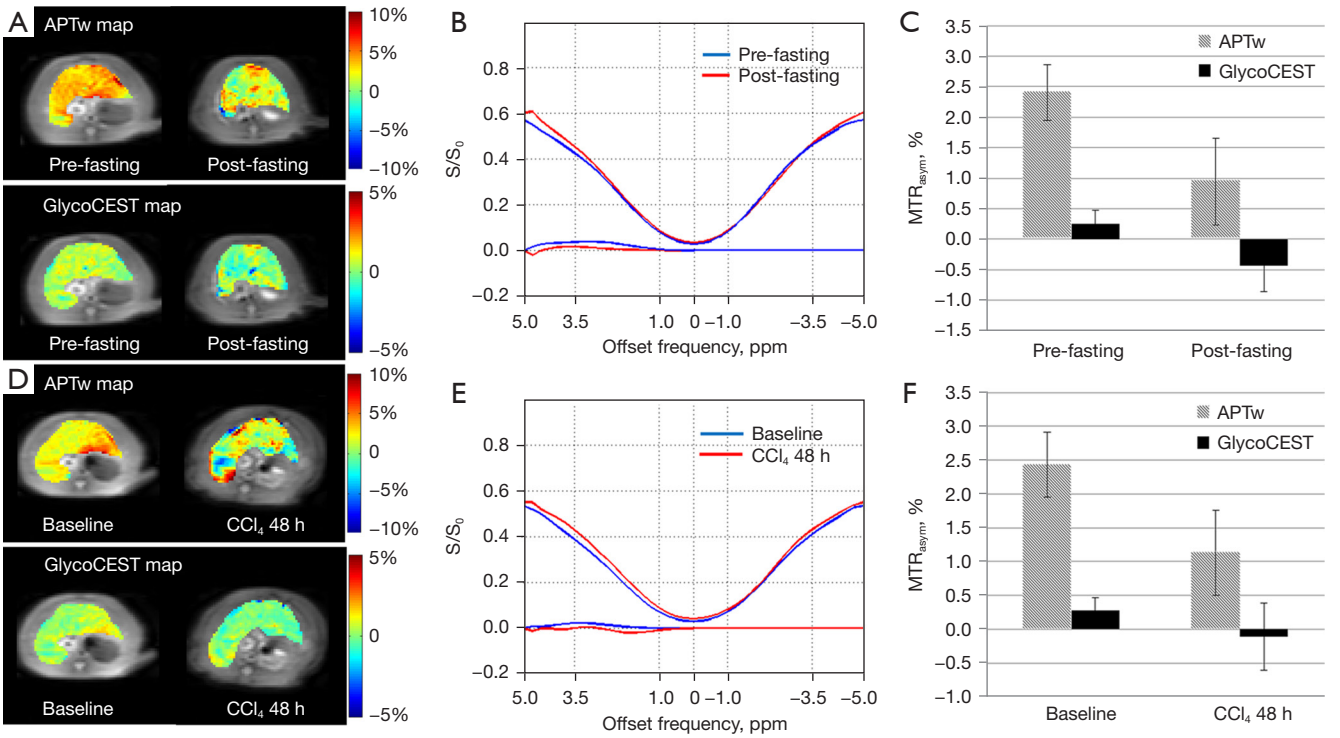

Figure 4 Typical APTw image and glycoCEST image (A) of a rat liver before and after 24-hour fasting with the corresponding ROI-averaged Z-spectrum and MTR_{asym} spectrum (B). In this rat, the APTw MTR_{asym} was 3.67% and the glycoCEST MTR_{asym} was 0.3% before 24-hour fasting. After 24-hour fasting, the APTw MTR_{asym} was 1.41% and the glycoCEST MTR_{asym} was 0.04%. (C) Bar plot of rat liver MTR_{asym} value of APTw and glycoCEST before and after 24-hour fasting (n=8). Typical APTw image and glycoCEST image (D) of a rat liver before and after CCl_4 injection with the corresponding ROI-averaged Z-spectrum and MTR_{asym} spectrum (E). In this rat, the baseline APTw MTR_{asym} was 2.66% and the glycoCEST MTR_{asym} was 0.56%. After 48-hour CCl_4 intoxication, the APTw MTR_{asym} was 1.91% and the glycoCEST MTR_{asym} was –0.05%. (F) Bar plot of rat liver MTR_{asym} value of APTw and glycoCEST before and after 48-hour CCl_4 injection (n=11). Reproduced with permission from Chen *et al.* (43). APTw, amide proton transfer-weighted; CEST, chemical exchange saturation transfer; glycoCEST, glycogen CEST; MTR_{asym}, asymmetrical magnetization transfer ratio; ROI, region of interest.

structures assumed due to an overexpressed protein related to cell division and cellular density. As APTw imaging may reflect cellular protein profiles and chemical properties of different focal liver lesions (FLLs), APTw imaging has been tested to help differentiate diseases such as focal FLLs.

After excluding patients with low image quality and small lesions (<1 cm), Lin *et al.* (47) studied 32 patients with hepatocellular carcinoma (HCC). Tumors were histologically classified from grade 1 to 4 according to the major Edmondson-Steiner grading, and grades 3 and 4 were considered high grade (n=19) while grades 1 and 2 were considered low grade (n=13). With a 3.0-T Philips MRI scanner, a single-slice CEST imaging was planned on the anatomical image showing the largest cross section of a solid tumor. APTw imaging was based on a single-shot turbo spin echo sequence. A pulse-train RF irradiation (saturation duration, 200 ms ×4; inter-pulse delay, 10 ms; saturation power, 2 μT) was applied. The 31 offsets included were 0, ±0.25, ±0.5, ±0.75, ±1, ±1.5, ±2, ±2.5, ±3.0, ±3.25, ±3.5, ±3.75, ±4, ±4.5, ±5.0, and ±6.0 ppm. The saturated image at the offset of 15.6 ppm was acquired to assess the conventional MT. The total acquisition time for the APTw imaging was 4 min and 21 s. The voxel-wise Z-spectrum was fitted by a 12th-order polynomial model, and the fitted curve was interpolated to a finer resolution of 1 Hz. The APT values were higher in the high-grade HCC (grades 3 and 4, 2.76%±1.38%) than in the low-grade HCC (grades 1 and 2, 1.59%±0.79%). Significant correlations were found between APTw values and histological grades. In differentiating high- from low-grade HCCs, area under

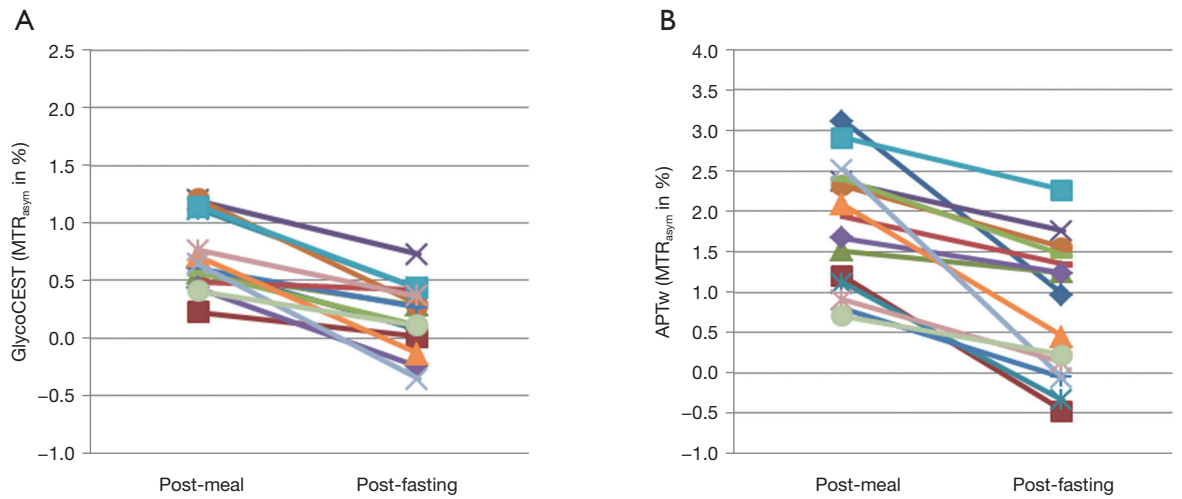

Figure 5 Line plot of liver MTR_{asym} value comparison between post-meal and post-fasting for glycoCEST (A) and APTw (B) (n=15). Reproduced with permission from Deng *et al.* (45). APTw, amide proton transfer-weighted; CEST, chemical exchange saturation transfer; glycoCEST, glycogen CEST; MTR_{asym}, asymmetrical magnetization transfer ratio.

the receiver operating characteristic curve (AUROC) was 0.81. The optimal APT cutoff value was 2.30%, and the corresponding sensitivity and specificity in the prediction of high-grade HCC were 92.3% and 68.4%, respectively. Furthermore, the conventional MT signal was quantified as: $MTR_{(15.6\ ppm)} = 1 - SI_{(15.6\ ppm)}/S_0$, and it was noted that no difference in $MTR_{(15.6\ ppm)}$ between high- and low-grade HCCs (13.2%±7.0% *vs.* 13.1%±13.4%) was found.

Wu *et al.* (48) studied 88 HCC patients, while excluding those with a low quality of MR images (n=3) and tumor lesions smaller than 1 cm (n=3). The mean tumor size was 7.82±3.65 cm, and according to the major Edmondson and Steiner grading system, patients were divided into four groups: grade 1 (G1, n=19), grade 2 (G2, n=30), grade 3 (G3, n=28), and grade 4 (G4, n=11). The same as above, G1 and G2, and G3 and G4 were defined as low- and high-grade HCC, respectively. MR scanning was done on a 3.0-T GE scanner. The APTw images were acquired through a single section that was selected as the one showing the maximum tumor area. CEST saturation sequence was a single-shot fast spin EPI sequence with free-breathing (Fermi pulses, with a power level of 2 μT and a total saturation duration of 2 s for four multiple pulses), and imaging was acquired with an EPI sequence. CEST imaging was repeated at 49 saturation frequency offsets (from 600 to −600 Hz with an interval of 25 Hz). In addition, three unsaturated images at the offset of 5,000 Hz were also acquired for signal normalization, which was 39 ppm away from water and other metabolites (±12 ppm) that can have CEST effect and was taken as water signal S_0 for calculation. APTw signal was 2.74%±1.27% for G1, 3.47%±1.02% for G2, 6.21%±2.66% for G3, and 7.53%±3.17% for G4, respectively. Pairwise comparisons revealed significant differences in APTw signals between G1 and G3, G1 and G4, G2 and G3, and G2 and G4. A moderate to good correlation was found between APTw signal and the histologic grade of HCC (R=0.679). The AUROC analyses demonstrated a good diagnostic performance of APTw signal (AUROC =0.890), for differentiating low- from high-grade HCC, with a sensitivity and specificity of 85.71% and 82.05%, respectively. Furthermore, Wu *et al.* (49) reported that APTw imaging may be more accurate than diffusion kurtosis imaging for predicting the histological grade of HCC.

Seo *et al.* (50) investigated the feasibility of using APTw imaging at 3.0 T to characterize FLLs. Two hundred and three patients with suspected FLLs were initially studied. A single slice including the largest area of the FLL was selected for APTw imaging, which was obtained using a single-slice turbo spin-echo sequence through five breath-holds. Saturation RF pulses were implemented using a series of four block RF pulses with 200 ms duration and 1.0 μT amplitude, each followed by a crusher gradient with 10 ms duration and 10 mT/m amplitude. Saturation frequency offsets were implemented at ±348, ±448, and ±548 Hz (±2.72, ±3.5, and ±4.28 ppm, respectively). A total

of 16 dynamics consisted of the dynamic loop, and the loop was split into five segments in which each segment was performed during a single breathhold containing APTw scans (turbo spin echo sequence) and a B_0 field map scan. One reference scan was acquired without saturation RF irradiation for signal normalization. Correction of the B_0 inhomogeneity was performed by measuring the inhomogeneity in the B_0 field map acquired with two-dimensional (2D) single-slice fast field-echo. Scan duration for each APT and B_0 field map sequence was 2 and 1.5 s, respectively, and then the duration for each breath-hold below 10 s. Total scan time was approximately 1 min plus the time between breath-holds. The technical success rate of APTw imaging in the liver was 62.1% (126/203). The reasons for failure were a too large B_0 inhomogeneity (n=43), significant respiratory motion (n=12), and these two factors together (n=22). Among 59 FLLs with analyzable APT images, MTR_{asym} values were compared between 27 patients with liver metastases and 23 patients with HCC, with the MTR_{asym} values of metastases significantly higher than those of HCC (0.13%±2.15% *vs.* –1.41%±3.68%, P=0.027). This study might have been limited by the low spectral resolution of the Z-spectrum.

More recently, Lin *et al.* (51) reported that APTw imaging combined with T2 mapping can improve the differential diagnosis of HCC and intrahepatic cholangiocarcinoma. APTw imaging, combined with T2 mapping, had a diagnostic efficacy with an AUROC of 0.91. Huang *et al.* (52) reported significantly different MTR_{asym} values between HCC and intrahepatic cholangiocarcinoma, with MTR_{asym} of HCC being higher than that of intrahepatic cholangiocarcinoma (1.40%±1.37% *vs.* 0.97%±1.22%, P=0.009).

From the same group as Wu *et al.* (48) and probably there are overlaps with the cases, Jia *et al.* (53) studied 56 patients with intermediate-stage HCC, with the goal to use APTw imaging to predict tumor to transarterial chemoembolization treatment (TACE). MRI was performed with a 3.0-T GE (General Electrics) MRI scanner. The data acquisition method was the same as Wu *et al.* (48). After TACE treatment, 28 patients showed tumor response and the remaining 28 patients did not exhibit tumor response. In the tumor tissue, the APTw signal of the response group (5.86%±2.36%) was significantly lower than that of the nonresponse group (7.67%±2.58%, P=0.009). Under multivariate analysis, tumor size, APTw signal, and IVIM-D_{slow} (tissue diffusion of intravoxel incoherent motion) of tumor tissue were identified as independent predictors for tumor response to TACE. AUROC for predicting tumor response to treatment was tumor size alone 0.67, IVIM-D_{slow} alone 0.76, and APTw signal 0.71. A combination of tumor size, APTw signal, and IVIM-D_{slow} had an AUROC of 0.85 (sensitivity: 0.71, specificity: 0.96).

Clinical 3.0-T scanner: tumor pHe measurement in human patients

Tang *et al.* (54) performed liver tumor pHe measurement using a 3.0-T GE MRI scanner. For *in vitro* experiments, using HCl and NaOH, five cylinders containing 50 mM ioversol were dissolved in phosphate-buffered saline. The prepared solution was titrated to pH values of 6.0, 6.4, 6.8, 7.2, and 7.6. The phantom was maintained at 37.0 ℃. A number of saturation pulses and flip angles were used to assess different pH values' influence on the CEST effect. CEST images were acquired with a gradient-echo readout, with presaturation applied by a Fermi pulse [16–32 ms and B_1 of 0.2–2.78 μT (50–850°)]. A total of 50 images were acquired, including 49 frequency offsets (0.25 ppm increment in saturation frequency) from 6 to –6 ppm and another S_0 image without saturation pulses. The B_0 correction method used the WASSR method (20). Phantom study confirmed that, at pH 6.0–7.2 the CEST effect gradually increased with an increase in pH, but then decreased at higher than pH 7.6. The results of four pre-saturation flip angles (flip =60, 150, 250, and 350°) showed the change in trend was consistent at the different flip angles. Finally, Ioversol pH MRI was performed at two flip angles of 60° (B_1=0.2 μT) and 350° (B_1=1.15 μT), using the ratiometric approach. For pH values ranging from 6.0 to 7.2, the CEST effects generated at the RF power corresponding to the 60° and 350° flip angles showed a strong correlation with the pH. Quantification of pH value via ioversol CEST imaging was ioversol concentration independent.

For the human study, Tang *et al.* included 15 HCC patients and five hepatic hemangioma patients. The scans were single slice acquisition. Fermi pulse with a width of 28 ms was set as the saturation pulse with two flip angles of 60° (B_1=0.2 μT) and 350° (B_1=1.15 μT). Compared with the *in vitro* study, to shorten the scan time, for *in-vivo* study 10 offset points (±5.25, ±5.5, ±5.75, ±6.0 ppm) were excluded and used the remaining 41 offsets (5 to –5 ppm) to produce CEST pH images. Intravenous ioversol (total: 105 mL) was administered at 1 mL/s for 60 s initially, then infused at 0.15 mL/s for 5 min during CEST data acquisition. Due to the presence of artifacts or incomplete acquisition, the

images of three patients failed the examination. The results demonstrated that the pHe value of tumor area was lower than that of the surrounding normal liver tissue (6.66±0.19 *vs.* 7.31±0.12, n=15, P<0.0001). Among hepatic hemangioma patients, the intensities of the ioversol signals in the CEST pHe analysis were consistent with those in the surrounding liver tissue (7.34±0.09 *vs.* 7.37±0.08, n=5), suggesting that hepatic hemangioma had a normal pHe value.

Current challenges for liver CEST imaging

Overall, the studies described in this editorial demonstrate the potential value of CEST imaging for liver disease. However, there are still many limitations. These reported studies probably 'proved the proof' of CEST imaging for the liver. These results have not been really translated into meaningful clinical application. To fulfill further translation into clinics, a number of issues remain to be overcome. The APTw imaging can be affected by fat (55), and the liver may have a higher fat fraction compared to lots of other organs. Chemical-shift selective lipid suppression should be implemented before the saturation section and turbo (fast) spin echo imaging readout. The amount of RF power deposition is a crucial point when using continuous wave RF radiation with multi-seconds long duration (for maximizing saturation effect). Clinical MRI scanners only allow limited saturation pulse duration as well as low duty cycle of RF amplifier, resulting in limited amount of RF power deposition to meet the Food and Drug Administration (FDA)-guided Specific Absorption Rate requirement. The RF pulse used for CEST clinical experiments is usually less powered or shortened, and the saturation efficiency might be compromised. Rather than the direct RF saturation scheme, several other methods for CEST effect preparation have been proposed, such as On resonance PARamagnetic CHemical Exchange Effects (OPARACHEE) (56) and frequency-labelled exchange transfer (FLEX) (57,58). Specifically designed on-resonance 360° RF pulse train with long duration and low power is applied in OPARACHEE. The resultant non-exchanging water protons will return back to z-axis, and exchanging protons from the solute pool will not experience a full 360° rotation, introducing a decreased magnetization in the z-axis. However, high sensitivity to B_1 and B_0 inhomogeneities as well as specific requirements to exchange rate and transverse relaxation rate might limit its wide applications in clinics. For FLEX, a series of labelling instead of saturation pulse modules are used for targeting exchanging protons. After solute protons transferring into the water pool, FLEX measures the modulation of water signal (i.e., free induction decay) based on the evolution of solute protons magnetization as a function of a so-called evolution time. However, similar to other CEST techniques, FLEX is also sensitive to B_0 inhomogeneities especially when applying diamagnetic CEST agents with close resonance frequencies relative to water, and to B_1 inhomogeneities affecting labelling efficiency.

Long scan time is an important limiting factor for wider validation and potential translation of the liver CEST technique. Till now, most of the reported studies only acquired a single slice through the liver. Of course, these sequences can be modified for multislice acquisitions, but scan duration may still limit the number of slices practical to patients. Sequences with radial or spiral k-space filling strategies for rapid acquisition have been tested for CEST imaging (59,60). Scan time can also be shortened if fewer frequency points are required for acquisition. Scheidegger *et al.* (61) described a sequence of saturation with frequency alternating RF irradiation (SAFARI) that requires short scan time for only three image acquisitions while keeping the specificity of CEST detection. However, this technique requires separate RF saturation pulses optimized for different chemical compounds to achieve the maximization of saturation of exchanging protons and minimization of DS. Moreover, the contribution of other compounds allocated nearby the target compounds remains challenging to be removed with SAFARI. Shah *et al.* (62) described a rapid CEST-fast imaging approach with steady-state free precession technique to provide CEST contrast in ~20 s. In one experimental study at 7.0 T, the CEST preparation was designed with a 5-s CEST pulse train [300 Gaussian pulses, BW_{RF} =300 Hz (1 ppm), peak B_1 amplitude =5 μT]. A fast imaging with steady state precession (FISP) sequence was used for liver coronal slice acquisition [TR: 3 ms, echo time (TE): 1.5 ms]. Thirteen coronal images were acquired by varying the center frequency of the CEST pulse train (10, 5, 4, 3, 2, 1, 0, –1, –2, –3, –4, –5, and –10 ppm). An additional CEST-FISP image was acquired at 90 ppm as a reference. The frequency sweep was repeated five times and retrospectively gated to generate a single data set. This technique provided CEST images in 5 s with fewer artifacts than conventional EPI readouts, and multiple CEST-weighted images were acquired within just a few minutes. The sensitivity of the CEST-fast imaging with steady-state free precession technique was also shown to be dependent on k-space encoding with centric k-space

encoding providing a 30–40% increase in CEST sensitivity relative to linear encoding for 256 or more k-space lines. As the CEST-FISP technique completely decouples the CEST preparation from the imaging readout, in theory the CEST preparation can be tailored practically to other field strengths and MT/CEST applications.

A number of fast CEST imaging methods reported for brain applications can potentially be adapted for liver studies. Acquisition-oriented methods that can be potentially adapted for liver imaging include GRASE (gradient- and spin-echo) CEST (63) and SPACE (sampling perfection with application optimized contrasts by using different flip angle evolutions) CEST (64) sequences. Zhu *et al.* (63) proposed the GRASE CEST sequence which deploys hybrid fast spin-echo and EPI readout as well as parallel imaging acceleration technique. The GRASE CEST sequence achieves faster acquisition than the most widely-used turbo spin-echo CEST, while avoiding a substantial part of the artifacts associated with EPI readout. It was demonstrated that whole-brain coverage with 26 saturation frequency offsets can be achieved with GRASE CEST in 8.7 min. Zhang *et al.* (64) proposed the SPACE CEST sequence also to achieve faster acquisition than the regular turbo spin-echo CEST method. In essence, SPACE CEST is an optimized version of turbo spin-echo CEST, with the main characteristics of non-selective slice encoding, shorter RF pulses, longer echo trains, and optional variable flip angle refocusing. Notably, the SPACE readout achieved an echo spacing of 3.4 ms, which was about half of that in the turbo spin-echo readout sequences previously reported for CEST imaging. Reconstruction-oriented methods that can be utilized for liver studies include variably-accelerated sensitivity encoding (vSENSE) (65,66) and compressed sensing (67,68). The vSENSE method proposed by Zhang *et al.* (65,66) utilized variable acceleration factors for different CEST frames. A low acceleration factor is selected for a reference frame to improve the sensitivity maps required in SENSE reconstruction with artifact suppression algorithms. Then, the other CEST frames can employ higher acceleration factors with the improved sensitivity maps to largely eliminate unfolding artifacts. Overall, vSENSE can achieve a higher acceleration factor than conventional SENSE. The compressed sensing methods can also be used to speed up CEST imaging. Compressed sensing capitalizes on the intrinsic sparsity in the CEST images either in the spatial or z-spectral domain. In conjunction with random incoherent undersampling and nonlinear iterative reconstruction, compressed sensing method promises to recover original high-quality image.

Data interpretation is another issue for CEST imaging. The measured CEST signal and contrast in tissue may be influenced by many factors, including but not limited to mobile proton content, proton exchange rate, tissue relaxation times, semi-solid MT, imaging protocol as well as quantification method. MTR_{asym} (3.5 ppm) is not a pure quantification due to various other contributions, such as the upfield NOE of aliphatic protons and some other CEST effects around 3.5 ppm. Particularly, at relatively low clinical field strengths like 3.0 T, the intrinsic low CEST signal level and the spill-over effect due to the small absolute chemical shift from water can reduce the accuracy and precision of the MTR_{asym} quantification. In addition, MTR_{asym} quantification is also subject to B_0 and B_1 inhomogeneities. As glycoCEST effect is closer to the water resonance, the MTR_{asym} values of glycoCEST are likely contaminated by direct saturation and MT effects under high power saturation. Thus, the predominant DS and MT effects can reduce the quantification accuracy of the small glycoCEST effect. In this aspect, a small saturation power should be useful to reduce the DS and MT. An off-resonance spin-lock pulse with a short irradiation duration may reduce the DS and offer higher sensitivity of glycoCEST effect. Fat suppression can induce extra water direct saturation and reduce the general image signal-to-noise ratio (SNR), and thus influence MTR_{asym} quantification, in particular for glycoCEST as its resonance is close to the water. WASSR is considered for better glycoCEST MTR_{asym} quantification via more accurate B_0 mapping (20). However, the WASSR acquisition and quantification might be highly sensitive to motion because of the low saturation strength and thus the sharp Z-spectrum. Furthermore, in the presence of an uneven respiration cycle, the use of WASSR-derived ΔB_0 map for Z-spectrum correction is technically challenging. Preclinical and clinical APTw MRI studies have usually attributed the altered APTw signal in tumors to an increase in cytosolic protein concentration because the cells are rapidly proliferating. This interpretation is also contested. Ray *et al.* (69) reported that the proportion of APTw MRI signal originating from changes in protein concentration was approximately 66%, with the remaining 34% could be from changes in tumor pH. Khlebnikov *et al.* (70) compared three different metrics of APTw contrast-magnetization transfer ratio (MTR_{Rex}), relaxation-compensated MTR_{Rex}, and traditional MTR_{asym} in normal and tumor tissues in a variety of intracranial tumors at 7.0 T. MTR_{Rex} and MTR_{asym} were calculated in the region of 3 to 4 ppm.

Relaxation-compensated MTR_{Rex} was calculated by water T1 relaxation correction of MTR_{Rex}. MTR_{Rex} and MTR_{asym} were slightly elevated in tumor-associated structures. Both metrics were positively correlated to water T1 relaxation. After water T1 relaxation correction, no difference between normal and tumor tissues was found for relaxation-compensated MTR_{Rex}. Khlebnikov *et al.* suggested that much of the APTw contrast in tumors for the low-power scheme at 7.0 T originates from the inherent tissue water T1-relaxation properties. For CEST image segmentation, Lin *et al.* (47) noted that the intrahepatic blood vessels showed hyperintensity on APTw images. By referring to routine structural MR images, APTw images can identify "hyperintensity artifacts", such as necrosis, hemorrhage, and vessels, which was necessary for accurate interpretation. The high-grade HCC signal was overall higher which might be contaminated by the increased blood vessels in high-grade tumors (47).

To better measure the NOE or 'pure' APT signal, a number of analysis approaches have been proposed. A mathematical method called extrapolated semisolid magnetization transfer reference (EMR) has been described for 'purer' APT ($APT^{\#}$) and NOE ($NOE^{\#}$) signal fitting (71,72). This method estimates a reference Z-spectrum (Z_{EMR}) of only direct saturation and MT effects by using the Z-spectrum intensities acquired at large frequency offsets where no CEST effect is expected. Using this method, a more specific APT effect has been reported in acute stroke and brain tumor studies, although $NOE^{\#}$ signal was still contaminated by the MT effect. APT and relayed NOE (rNOE) signals can be fitted pixelwise using multiple Lorentzian functions (73). The corresponding label (Z_{lab}) as well as a reference Z-spectrum (Z_{ref}) can be obtained for separate APT and rNOE effects. To additionally compensate for the relaxation time, a method called apparent exchange-dependent relaxation (AREX) has been used (73-75). Cubic-spline interpolation has been reported to improve MTR_{asym} quantification particularly for CEST images with low SNR (76). This method may be useful in studies when lower saturation strength is used with low number of excitations (NEX).

In conclusion, a number of studies on liver CEST imaging have been reported. Compared with liver parenchyma, liver tumors with higher regeneration potential were noted to have higher APTw signal, and malignant liver tumors were shown to be acidic with a lower pHe value. GlycoCEST measures liver glycogen level, with the liver at fasted status having a lower glycoCEST signal. APTw CEST has also been tested to assess liver fibrosis. However, there are still many limitations. These studies probably 'proved the proof' of CEST imaging for the liver, and have not been really translated into meaningful clinical application. Further technical improvements to optimize CEST imaging protocols and to overcome B_0 field inhomogeneity, and a good interpretation of data, are required. MRI can potentially provide a multi-contrast and multi-parametric approach to diagnosis and evaluate liver diseases. Other techniques such as contrast enhanced imaging, diffusion-weighted imaging (including intravoxel incoherent motion analysis), quantitative susceptibility mapping, elastography, native T1 mapping, T1rho mapping, macromolecular fraction mapping, etc. are also being tested for evaluation of the liver (77-87). A combination of multiple techniques shall eventually allow a comprehensive evaluation of liver function and tissue/lesion characterization.

Acknowledgments

Funding: This work was partially supported by Hong Kong GRF Projects (Nos. 14109218 and 14112521).

Footnote

Provenance and Peer Review: This article was a standard submission to the journal. The article has undergone external peer review.

Conflicts of Interest: All authors have completed the ICMJE uniform disclosure form (available at https://qims.amegroups.com/article/view/10.21037/qims-23-379/coif). YXJW serves as the Editor-in-Chief of *Quantitative Imaging in Medicine and Surgery*. WD is an employee of GE Healthcare. ZS is an employee of Philips Healthcare. YZ and colleagues developed SPACE CEST sequence and vSENSE described in this article. The authors have no other conflicts of interest to declare.

Ethical Statement: The authors are accountable for all aspects of the work in ensuring that questions related to the accuracy or integrity of any part of the work are appropriately investigated and resolved.

References

1. Henkelman RM, Stanisz GJ, Graham SJ. Magnetization transfer in MRI: a review. NMR Biomed 2001;14:57-64.
2. Ward KM, Aletras AH, Balaban RS. A new class of contrast agents for MRI based on proton chemical exchange dependent saturation transfer (CEST). J Magn Reson 2000;143:79-87.
3. Zaiss M, Bachert P. Chemical exchange saturation transfer (CEST) and MR Z-spectroscopy in vivo: a review of theoretical approaches and methods. Phys Med Biol 2013;58:R221-69.
4. Vinogradov E, Sherry AD, Lenkinski RE. CEST: from basic principles to applications, challenges and opportunities. J Magn Reson 2013;229:155-72.
5. Wu B, Warnock G, Zaiss M, Lin C, Chen M, Zhou Z, Mu L, Nanz D, Tuura R, Delso G. An overview of CEST MRI for non-MR physicists. EJNMMI Phys 2016;3:19.
6. Zhou J, Lal B, Wilson DA, Laterra J, van Zijl PC. Amide proton transfer (APT) contrast for imaging of brain tumors. Magn Reson Med 2003;50:1120-6.
7. Dou W, Lin CE, Ding H, Shen Y, Dou C, Qian L, Wen B, Wu B. Chemical exchange saturation transfer magnetic resonance imaging and its main and potential applications in pre-clinical and clinical studies. Quant Imaging Med Surg 2019;9:1747-66.
8. Qamar S, King AD, Ai QH, Mo FKF, Chen W, Poon DMC, Tong M, Ma BB, Yeung DK, Wang YX, Yuan J. Pre-treatment amide proton transfer imaging predicts treatment outcome in nasopharyngeal carcinoma. Eur Radiol 2020;30:6339-47.
9. Qamar S, King AD, Ai QY, Law BKH, Chan JSM, Poon DMC, Tong M, Mo FKF, Chen W, Bhatia KS, Ahuja AT, Ma BBY, Yeung DK, Wang YX, Yuan J. Amide proton transfer MRI detects early changes in nasopharyngeal carcinoma: providing a potential imaging marker for treatment response. Eur Arch Otorhinolaryngol 2019;276:505-12.
10. Zhou J, Zaiss M, Knutsson L, Sun PZ, Ahn SS, Aime S, et al. Review and consensus recommendations on clinical APT-weighted imaging approaches at 3T: Application to brain tumors. Magn Reson Med 2022;88:546-74.
11. Lucas A, Nanga RPR, Hadar P, Chen S, Gibson A, Oechsel K, Elliott MA, Stein JM, Das S, Reddy R, Detre JA, Davis KA. Mapping hippocampal glutamate in mesial temporal lobe epilepsy with glutamate weighted CEST (GluCEST) imaging. Hum Brain Mapp 2023;44:549-58.
12. Takahashi Y, Saito S, Kioka H, Araki R, Asano Y, Takashima S, Sakata Y, Yoshioka Y. Mouse skeletal muscle creatine chemical exchange saturation transfer (CrCEST) imaging at 11.7T MRI. J Magn Reson Imaging 2020;51:563-70.
13. Deng M, Yuan J, Chen WT, Chan Q, Griffith JF, Wang YX. Evaluation of Glycosaminoglycan in the Lumbar Disc Using Chemical Exchange Saturation Transfer MR at 3.0 Tesla: Reproducibility and Correlation with Disc Degeneration. Biomed Environ Sci 2016;29:47-55.
14. Soellner ST, Welsch GH, Gelse K, Goldmann A, Kleyer A, Schett G, Pachowsky ML. gagCEST imaging at 3 T MRI in patients with articular cartilage lesions of the knee and intraoperative validation. Osteoarthritis Cartilage 2021;29:1163-72.
15. Liepinsh E, Otting G. Proton exchange rates from amino acid side chains--implications for image contrast. Magn Reson Med 1996;35:30-42.
16. Jones CK, Huang A, Xu J, Edden RA, Schär M, Hua J, Oskolkov N, Zacà D, Zhou J, McMahon MT, Pillai JJ, van Zijl PC. Nuclear Overhauser enhancement (NOE) imaging in the human brain at 7T. Neuroimage 2013;77:114-24.
17. Li H, Zu Z, Zaiss M, Khan IS, Singer RJ, Gochberg DF, Bachert P, Gore JC, Xu J. Imaging of amide proton transfer and nuclear Overhauser enhancement in ischemic stroke with corrections for competing effects. NMR Biomed 2015;28:200-9.
18. Zhou J, Hong X, Zhao X, Gao JH, Yuan J. APT-weighted and NOE-weighted image contrasts in glioma with different RF saturation powers based on magnetization transfer ratio asymmetry analyses. Magn Reson Med 2013;70:320-7.
19. Sun PZ. Quasi-steady state chemical exchange saturation transfer (QUASS CEST) analysis-correction of the finite relaxation delay and saturation time for robust CEST measurement. Magn Reson Med 2021;85:3281-9.
20. Kim M, Gillen J, Landman BA, Zhou J, van Zijl PC. Water saturation shift referencing (WASSR) for chemical exchange saturation transfer (CEST) experiments. Magn Reson Med 2009;61:1441-50.
21. Schuenke P, Windschuh J, Roeloffs V, Ladd ME, Bachert

P, Zaiss M. Simultaneous mapping of water shift and B(1) (WASABI)-Application to field-Inhomogeneity correction of CEST MRI data. Magn Reson Med 2017;77:571-80.
22. Chan KW, McMahon MT, Kato Y, Liu G, Bulte JW, Bhujwalla ZM, Artemov D, van Zijl PC. Natural D-glucose as a biodegradable MRI contrast agent for detecting cancer. Magn Reson Med 2012;68:1764-73.
23. Xu X, Yadav NN, Knutsson L, Hua J, Kalyani R, Hall E, Laterra J, Blakeley J, Strowd R, Pomper M, Barker P, Chan K, Liu G, McMahon MT, Stevens RD, van Zijl PC. Dynamic Glucose-Enhanced (DGE) MRI: Translation to Human Scanning and First Results in Glioma Patients. Tomography 2015;1:105-14.
24. Yuan J, Zhou J, Ahuja AT, Wang YX. MR chemical exchange imaging with spin-lock technique (CESL): a theoretical analysis of the Z-spectrum using a two-pool R(1ρ) relaxation model beyond the fast-exchange limit. Phys Med Biol 2012;57:8185-200.
25. Jin T, Iordanova B, Hitchens TK, Modo M, Wang P, Mehrens H, Kim SG. Chemical exchange-sensitive spin-lock (CESL) MRI of glucose and analogs in brain tumors. Magn Reson Med 2018;80:488-95.
26. Schuenke P, Paech D, Koehler C, Windschuh J, Bachert P, Ladd ME, Schlemmer HP, Radbruch A, Zaiss M. Fast and Quantitative T1ρ-weighted Dynamic Glucose Enhanced MRI. Sci Rep 2017;7:42093.
27. Paech D, Schuenke P, Koehler C, Windschuh J, Mundiyanapurath S, Bickelhaupt S, Bonekamp D, Bäumer P, Bachert P, Ladd ME, Bendszus M, Wick W, Unterberg A, Schlemmer HP, Zaiss M, Radbruch A. T1ρ-weighted Dynamic Glucose-enhanced MR Imaging in the Human Brain. Radiology 2017;285:914-22.
28. van Zijl PC, Jones CK, Ren J, Malloy CR, Sherry AD. MRI detection of glycogen in vivo by using chemical exchange saturation transfer imaging (glycoCEST). Proc Natl Acad Sci U S A 2007;104:4359-64.
29. Sagiyama K, Zhang S, Dimitrov I, Sherry AD, Takahashi M. In Vivo Monitoring of Liver Glycogen by Chemical Exchange Saturation Transfer Imaging (GlycoCEST) in Live Mice. Proc Intl Soc Mag Reson Med 2014;22: abstr 0762.
30. Miller CO, Cao J, Chekmenev EY, Damon BM, Cherrington AD, Gore JC. Noninvasive measurements of glycogen in perfused mouse livers using chemical exchange saturation transfer NMR and comparison to (13)C NMR spectroscopy. Anal Chem 2015;87:5824-30.
31. Ren J, Trokowski R, Zhang S, Malloy CR, Sherry AD. Imaging the tissue distribution of glucose in livers using a PARACEST sensor. Magn Reson Med 2008;60:1047-55.
32. Shoulders MD, Raines RT. Collagen structure and stability. Annu Rev Biochem 2009;78:929-58.
33. Bataller R, Brenner DA. Liver fibrosis. J Clin Invest 2005;115:209-18.
34. Lindquist DM, Fugate EM, Wang J, Sharma A, Gandhi CR, Dillman JR. MRI Measures of Murine Liver Fibrosis. J Magn Reson Imaging 2021;54:739-49.
35. Griffiths JR. Are cancer cells acidic? Br J Cancer 1991;64:425-7.
36. Gatenby RA, Gillies RJ. Why do cancers have high aerobic glycolysis? Nat Rev Cancer 2004;4:891-9.
37. Estrella V, Chen T, Lloyd M, Wojtkowiak J, Cornnell HH, Ibrahim-Hashim A, Bailey K, Balagurunathan Y, Rothberg JM, Sloane BF, Johnson J, Gatenby RA, Gillies RJ. Acidity generated by the tumor microenvironment drives local invasion. Cancer Res 2013;73:1524-35.
38. Ward KM, Balaban RS. Determination of pH using water protons and chemical exchange dependent saturation transfer (CEST). Magn Reson Med 2000;44:799-802.
39. Longo DL, Dastrù W, Digilio G, Keupp J, Langereis S, Lanzardo S, Prestigio S, Steinbach O, Terreno E, Uggeri F, Aime S. Iopamidol as a responsive MRI-chemical exchange saturation transfer contrast agent for pH mapping of kidneys: In vivo studies in mice at 7 T. Magn Reson Med 2011;65:202-11.
40. Longo DL, Michelotti F, Consolino L, Bardini P, Digilio G, Xiao G, Sun PZ, Aime S. In vitro and In Vivo Assessment of Nonionic Iodinated Radiographic Molecules as Chemical Exchange Saturation Transfer Magnetic Resonance Imaging Tumor Perfusion Agents. Invest Radiol 2016;51:155-62.
41. Chen M, Chen C, Shen Z, Zhang X, Chen Y, Lin F, Ma X, Zhuang C, Mao Y, Gan H, Chen P, Zong X, Wu R. Extracellular pH is a biomarker enabling detection of breast cancer and liver cancer using CEST MRI. Oncotarget 2017;8:45759-67.
42. Longo DL, Sun PZ, Consolino L, Michelotti FC, Uggeri F, Aime S. A general MRI-CEST ratiometric approach for pH imaging: demonstration of in vivo pH mapping with iobitridol. J Am Chem Soc 2014;136:14333-6.
43. Chen SZ, Yuan J, Deng M, Wei J, Zhou J, Wáng YX. Chemical exchange saturation transfer (CEST) MR technique for in-vivo liver imaging at 3.0 tesla. Eur Radiol 2016;26:1792-800.
44. Muriel P. Nitric oxide protection of rat liver from lipid peroxidation, collagen accumulation, and liver damage induced by carbon tetrachloride. Biochem Pharmacol

1998;56:773-9.
45. Deng M, Chen SZ, Yuan J, Chan Q, Zhou J, Wáng YX. Chemical Exchange Saturation Transfer (CEST) MR Technique for Liver Imaging at 3.0 Tesla: an Evaluation of Different Offset Number and an After-Meal and Over-Night-Fast Comparison. Mol Imaging Biol 2016;18:274-82.
46. Lu J, Zhou J, Cai C, Cai S, Chen Z. Observation of true and pseudo NOE signals using CEST-MRI and CEST-MRS sequences with and without lipid suppression. Magn Reson Med 2015;73:1615-22.
47. Lin Y, Luo X, Yu L, Zhang Y, Zhou J, Jiang Y, Zhang C, Zhang J, Li C, Chen M. Amide proton transfer-weighted MRI for predicting histological grade of hepatocellular carcinoma: comparison with diffusion-weighted imaging. Quant Imaging Med Surg 2019;9:1641-51.
48. Wu B, Jia F, Li X, Li L, Wang K, Han D. Comparative Study of Amide Proton Transfer Imaging and Intravoxel Incoherent Motion Imaging for Predicting Histologic Grade of Hepatocellular Carcinoma. Front Oncol 2020;10:562049.
49. Wu B, Jia F, Li X, Zhang M, Han D, Jia Z. Amide Proton Transfer Imaging vs Diffusion Kurtosis Imaging for Predicting Histological Grade of Hepatocellular Carcinoma. J Hepatocell Carcinoma 2020;7:159-68.
50. Seo N, Jeong HK, Choi JY, Park MS, Kim MJ, Chung YE. Liver MRI with amide proton transfer imaging: feasibility and accuracy for the characterization of focal liver lesions. Eur Radiol 2021;31:222-31.
51. Lin T, Wang J, Wu Z, Chen L, Song Q, Pu R, Ying Zhao Y, Xue Ren X, Xu Q, Liu A. Improved differentiation of Primaray liver cancer by combination of Amide Transfer weighted imaging(APTw) and T2 mapping. Proc Intl Soc Mag Reson Med 2022;31:abstr 4290.
52. Huang J, Chen J, Dou W, Ye J, Xia W, Luo X. Amide proton transfer weighted imaging in differential diagnosis of hepatocellular carcinoma from intrahepatic cholangiocarcinoma. Proc Intl Soc Mag Reson Med 2022;31:abstr 3816.
53. Jia F, Wu B, Yan R, Li L, Wang K, Han D. Prediction Model for Intermediate-Stage Hepatocellular Carcinoma Response to Transarterial Chemoembolization. J Magn Reson Imaging 2020;52:1657-67.
54. Tang Y, Xiao G, Shen Z, Zhuang C, Xie Y, Zhang X, Yang Z, Guan J, Shen Y, Chen Y, Lai L, Chen Y, Chen S, Dai Z, Wang R, Wu R. Noninvasive Detection of Extracellular pH in Human Benign and Malignant Liver Tumors Using CEST MRI. Front Oncol 2020;10:578985.
55. Zimmermann F, Korzowski A, Breitling J, Meissner JE, Schuenke P, Loi L, Zaiss M, Bickelhaupt S, Schott S, Schlemmer HP, Paech D, Ladd ME, Bachert P, Goerke S. A novel normalization for amide proton transfer CEST MRI to correct for fat signal-induced artifacts: application to human breast cancer imaging. Magn Reson Med 2020;83:920-34.
56. Vinogradov E, He H, Lubag A, Balschi JA, Sherry AD, Lenkinski RE. MRI detection of paramagnetic chemical exchange effects in mice kidneys in vivo. Magn Reson Med 2007;58:650-5.
57. Friedman JI, McMahon MT, Stivers JT, Van Zijl PC. Indirect detection of labile solute proton spectra via the water signal using frequency-labeled exchange (FLEX) transfer. J Am Chem Soc 2010;132:1813-5.
58. Lin CY, Yadav NN, Friedman JI, Ratnakar J, Sherry AD, van Zijl PC. Using frequency-labeled exchange transfer to separate out conventional magnetization transfer effects from exchange transfer effects when detecting ParaCEST agents. Magn Reson Med 2012;67:906-11.
59. Sui R, Chen L, Li Y, Huang J, Chan KWY, Xu X, van Zijl PCM, Xu J. Whole-brain amide CEST imaging at 3T with a steady-state radial MRI acquisition. Magn Reson Med 2021;86:893-906.
60. High RA, Ji Y, Ma YJ, Tang Q, Murphy ME, Du J, Chang EY. In vivo assessment of extracellular pH of joint tissues using acidoCEST-UTE MRI. Quant Imaging Med Surg 2019;9:1664-73.
61. Scheidegger R, Vinogradov E, Alsop DC. Amide proton transfer imaging with improved robustness to magnetic field inhomogeneity and magnetization transfer asymmetry using saturation with frequency alternating RF irradiation. Magn Reson Med 2011;66:1275-85.
62. Shah T, Lu L, Dell KM, Pagel MD, Griswold MA, Flask CA. CEST-FISP: a novel technique for rapid chemical exchange saturation transfer MRI at 7 T. Magn Reson Med 2011;65:432-7.
63. Zhu H, Jones CK, van Zijl PC, Barker PB, Zhou J. Fast 3D chemical exchange saturation transfer (CEST) imaging of the human brain. Magn Reson Med 2010;64:638-44.
64. Zhang Y, Yong X, Liu R, Tang J, Jiang H, Fu C, Wei R, Hsu YC, Sun Y, Luo B, Wu D. Whole-brain chemical exchange saturation transfer imaging with optimized turbo spin echo readout. Magn Reson Med 2020;84:1161-72.
65. Zhang Y, Heo HY, Lee DH, Jiang S, Zhao X, Bottomley PA, Zhou J. Chemical exchange saturation transfer (CEST) imaging with fast variably-accelerated sensitivity encoding (vSENSE). Magn Reson Med 2017;77:2225-38.

66. Zhang Y, Heo HY, Jiang S, Zhou J, Bottomley PA. Fast 3D chemical exchange saturation transfer imaging with variably-accelerated sensitivity encoding (vSENSE). Magn Reson Med 2019;82:2046-61.
67. Heo HY, Zhang Y, Lee DH, Jiang S, Zhao X, Zhou J. Accelerating chemical exchange saturation transfer (CEST) MRI by combining compressed sensing and sensitivity encoding techniques. Magn Reson Med 2017;77:779-86.
68. Heo HY, Xu X, Jiang S, Zhao Y, Keupp J, Redmond KJ, Laterra J, van Zijl PCM, Zhou J. Prospective acceleration of parallel RF transmission-based 3D chemical exchange saturation transfer imaging with compressed sensing. Magn Reson Med 2019;82:1812-21.
69. Ray KJ, Simard MA, Larkin JR, Coates J, Kinchesh P, Smart SC, Higgins GS, Chappell MA, Sibson NR. Tumor pH and Protein Concentration Contribute to the Signal of Amide Proton Transfer Magnetic Resonance Imaging. Cancer Res 2019;79:1343-52.
70. Khlebnikov V, Polders D, Hendrikse J, Robe PA, Voormolen EH, Luijten PR, Klomp DW, Hoogduin H. Amide proton transfer (APT) imaging of brain tumors at 7 T: The role of tissue water T(1) -Relaxation properties. Magn Reson Med 2017;77:1525-32.
71. Heo HY, Zhang Y, Lee DH, Hong X, Zhou J. Quantitative assessment of amide proton transfer (APT) and nuclear overhauser enhancement (NOE) imaging with extrapolated semi-solid magnetization transfer reference (EMR) signals: Application to a rat glioma model at 4.7 Tesla. Magn Reson Med 2016;75:137-49.
72. Heo HY, Zhang Y, Jiang S, Lee DH, Zhou J. Quantitative assessment of amide proton transfer (APT) and nuclear overhauser enhancement (NOE) imaging with extrapolated semisolid magnetization transfer reference (EMR) signals: II. Comparison of three EMR models and application to human brain glioma at 3 Tesla. Magn Reson Med 2016;75:1630-9.
73. Zaiss M, Windschuh J, Paech D, Meissner JE, Burth S, Schmitt B, Kickingereder P, Wiestler B, Wick W, Bendszus M, Schlemmer HP, Ladd ME, Bachert P, Radbruch A. Relaxation-compensated CEST-MRI of the human brain at 7T: Unbiased insight into NOE and amide signal changes in human glioblastoma. Neuroimage 2015;112:180-8.
74. Zaiss M, Xu J, Goerke S, Khan IS, Singer RJ, Gore JC, Gochberg DF, Bachert P. Inverse Z-spectrum analysis for spillover-, MT-, and T1 -corrected steady-state pulsed CEST-MRI--application to pH-weighted MRI of acute stroke. NMR Biomed 2014;27:240-52.
75. Zaiss M, Windschuh J, Goerke S, Paech D, Meissner JE, Burth S, Kickingereder P, Wick W, Bendszus M, Schlemmer HP, Ladd ME, Bachert P, Radbruch A. Downfield-NOE-suppressed amide-CEST-MRI at 7 Tesla provides a unique contrast in human glioblastoma. Magn Reson Med 2017;77:196-208.
76. Stancanello J, Terreno E, Castelli DD, Cabella C, Uggeri F, Aime S. Development and validation of a smoothing-splines-based correction method for improving the analysis of CEST-MR images. Contrast Media Mol Imaging 2008;3:136-49.
77. Ringe KI, Yoon JH. Strategies and Techniques for Liver Magnetic Resonance Imaging: New and Pending Applications for Routine Clinical Practice. Korean J Radiol 2023;24:180-9. Erratum in: Korean J Radiol. 2023 Apr;24(4):372-373.
78. Wáng YXJ, Wang X, Wu P, Wang Y, Chen W, Chen H, Li J. Topics on quantitative liver magnetic resonance imaging. Quant Imaging Med Surg 2019;9:1840-90.
79. Wang YXJ, Huang H, Zheng CJ, Xiao BH, Chevallier O, Wang W. Diffusion-weighted MRI of the liver: challenges and some solutions for the quantification of apparent diffusion coefficient and intravoxel incoherent motion. Am J Nucl Med Mol Imaging 2021;11:107-42.
80. Wang C, Yuan XD, Wu N, Sun WR, Tian Y. Optimization of hepatobiliary phase imaging in gadoxetic acid-enhanced magnetic resonance imaging: a narrative review. Quant Imaging Med Surg 2023;13:1972-82.
81. Schambeck JPL, Forte GC, Gonçalves LM, Stuker G, Kotlinski JBF, Tramontin G, Altmayer S, Watte G, Hochhegger B. Diagnostic accuracy of magnetic resonance elastography and point-shear wave elastography for significant hepatic fibrosis screening: Systematic review and meta-analysis. PLoS One 2023;18:e0271572.
82. Wang YX, Yuan J. Evaluation of liver fibrosis with T1ρ MR imaging. Quant Imaging Med Surg 2014;4:152-5.
83. Gursan A, Prompers JJ. Magnetic Resonance Imaging and Spectroscopy Methods to Study Hepatic Glucose Metabolism and Their Applications in the Healthy and Diabetic Liver. Metabolites 2022.
84. Wáng YXJ, Deng M, Li YT, Huang H, Leung JCS, Chen W, Lu PX. A Combined Use of Intravoxel Incoherent Motion MRI Parameters Can Differentiate Early-Stage Hepatitis-b Fibrotic Livers from Healthy Livers. SLAS Technol 2018;23:259-68.
85. Kim JW, Lee YS, Park YS, Kim BH, Lee SY, Yeon JE, Lee CH. Multiparametric MR Index for the Diagnosis of Non-Alcoholic Steatohepatitis in Patients with Non-Alcoholic

Fatty Liver Disease. Sci Rep 2020;10:2671.
86. Mesropyan N, Kupczyk P, Dold L, Weismüller TJ, Sprinkart AM, Mädler B, Pieper CC, Kuetting D, Strassburg CP, Attenberger U, Luetkens JA. Non-invasive assessment of liver fibrosis in autoimmune hepatitis: Diagnostic value of liver magnetic resonance parametric mapping including extracellular volume fraction. Abdom Radiol (NY) 2021;46:2458-66.
87. Yarnykh VL, Tartaglione EV, Ioannou GN. Fast macromolecular proton fraction mapping of the human liver in vivo for quantitative assessment of hepatic fibrosis. NMR Biomed 2015;28:1716-25.

Cite this article as: Wáng YXJ, Dou W, Shen Z, Zhang Y. An update on liver chemical exchange saturation transfer imaging with a focus on clinical translation. Quant Imaging Med Surg 2023;13(7):4057-4076. doi: 10.21037/qims-23-379

